Remote Sensing of Environment 138 (2013) 10–18

Contents lists available at SciVerse ScienceDirect

Remote Sensing of Environment

journal homepage: www.elsevier.com/locate/rse

Surface deformation detected by ALOS PALSAR small baseline SAR interferometry over permafrost environment of Beiluhe section, Tibet Plateau, China

Fulong Chen [a,b,*], Hui Lin [c,d], Wei Zhou [a,b], Tianhua Hong [b], Gang Wang [a]

[a] Key Laboratory of Digital Earth Science, Institute of Remote Sensing and Digital Earth, Chinese Academy of Sciences, No. 9 Dengzhuang South Road, Haidian District, Beijing 100094, China
[b] International Centre on Space Technologies for Natural and Cultural Heritage under the Auspices of UNESCO, No. 9 Dengzhuang South Road, Haidian District, Beijing 100094, China
[c] Institute of Space and Earth Information Science, The Chinese University of Hong Kong, Shatin, N.T., Hong Kong, China
[d] Department of Geography and Resource Management, The Chinese University of Hong Kong, ShaTin, N.T., Hong Kong, China

ARTICLE INFO

Article history:
Received 4 January 2013
Received in revised form 4 July 2013
Accepted 6 July 2013
Available online xxxx

Keywords:
Small BAseline Subsets
Permafrost
Tibet Plateau
Qinghai–Tibet Railway
Natural reserve

ABSTRACT

The evolution of permafrost and the active layer is highly related to biological diversity and climate change because of its feedback effects involving water and carbon storage. In this study, we firstly examined the relationship of active layer variation, geomorphological processes and anthropogenic activities by means of small baseline synthetic aperture radar interferometry in Beiluhe, Hoh Xil natural reserve in Tibet Plateau (TP), China. 3.5-Yr observation span of L-band ALOS PALSAR data (June, 2007 to December, 2010) was used. The estimated surface displacements (primarily in the range of -20 mm yr^{-1} to 20 mm yr^{-1}) and time-series implied evolution of the active layer and permafrost beneath. The motion trend along slopes was complicated due to the geomorphological processes, and thus interdisciplinary interpretations were needed. Anthropogenic influences on this frail permafrost environment were significant, as evident from the remarkable surface settlement along the embankment of Qinghai–Tibet Railway. It is crucial and necessary to monitor this permafrost plateau owing to the consequences arising from a combination of factors related to climate change, geo-hazard prediction, nature conservation and regional sustainable development.

1. Introduction

The Tibet Plateau (TP), recognized as the third pole of Earth, has the largest extent of permafrost outside the Polar Regions (Kang et al., 2010). Permafrost is sensitive to global warming, resulting in significant influences on regional water balance, biological diversity, carbon cycle and engineering constructions. TP, known as the Asia water tower, is the source region of many major rivers in Asia (Immerzeel, Stoorvogel, & Antle, 2008). The perennial flow of those rivers largely relies on the constant flux from melting glaciers. Approximately 23–48% of the total global soil carbon pool is stored in permafrost regions in the world (Guo & Macdonald, 2006; Tarnocai et al., 2009). Thus carbon emission from permafrost when it thaws under global warming is a major concern (Monastersky, 2011; Schuur et al., 2008). The active layer overlaid on permafrost tends to be unstable due to the dynamics of frost heave and thaw settlement. As the plateau is being developed, anthropogenic activities, such as expansive natural resource exploitation and tourism, have introduced external pressures on the local environment and biological diversity. All issues described above are closely correlated with the dynamics of the active layer as well as the permafrost beneath.

As the terrestrial unit at the highest elevation, many of studies have been conducted in TP because of its significance for global and regional sustainable development, including climate change consequences and impacts of carbon emissions (Liu, Wang, Yu, Yang, & Zhang, 2009; Wu, Jiang, & Zhang, 2010), tectonics and earthquakes (Ismail-Zadeh, Mouel, Soloviev, Tapponnier, & Vorovieva, 2007; Loveless & Meade, 2011; Qiao, Yang, Du, Ge, & Wang, 2011), water balance (Niu, Lin, Liu, & Lu, 2011; Wang, Hu, & Li, 2009; Wang, Li, Hu, & Li, 2009) and the future of the permafrost environment (Jin, Yu, Wang, & Lu, 2008; Wu & Zhang, 2008, 2010; Yang et al., 2004). However, the surface movement surveillance over this permafrost environment using spaceborne Synthetic Aperture Radar Interferometry (InSAR) is still in its early stages. For instance, Chen, Lin, Li, Chen, and Zhou (2012) exploited the stability of the embankment of Qinghai–Tibet Railway by an improved Interferometric Point Target Analysis (IPTA) approach jointly using C- and L-band SAR data. Surface evolution in other parts of the TP is still not well-known. Differential InSAR (DInSAR), one of the quantitative remote sensing technologies, has proved to be effective for subtle motion detection by measuring the phase difference of two or multi-temporal SAR acquisitions (Massonnet et al., 1993; Usai & Klees, 1999). The Multi-Temporal SAR Interferometry (MT-InSAR) mitigates the intrinsic limitations of the traditional DInSAR (spatial–temporal decorrelation as

* Corresponding author at: Key Laboratory of Digital Earth Science, Institute of Remote Sensing and Digital Earth, Chinese Academy of Sciences, No. 9 Dengzhuang South Road, Haidian District, Beijing 100094, China. Tel.: +86 10 82178198; fax: +86 10 82178915.
E-mail address: chenfulong@ceode.ac.cn (F. Chen).

0034-4257/$ – see front matter © 2013 Elsevier Inc. All rights reserved.
http://dx.doi.org/10.1016/j.rse.2013.07.006

well as atmospheric disturbance) by analyzing a large dataset of SAR images over the same area; and thus is capable of deriving surface motion rates with accuracy at the millimeter level. In general, MT-InSAR can be divided into three main categories: Persistent Scatterer (PS) (Chen & Lin, 2011; Ferretti, Prati, & Rocca, 2000; Hooper, Bekaert, Spaans, & Arkan, 2012; Hooper, Zebker, Segall, & Kampes, 2004), Small BAseline Subsets (SBAS) (Berardino, Fornaro, Lanari, & Sansosti, 2002; Chen, Lin, Yeung, & Cheng, 2010; Chen, Lin, Zhang, & Lu, 2012; Jiang, Lin, Ma, Kong, & Wang, 2011; Lanari, Mora, & Manunta, 2004; Lin, Chen, & Zhao, 2011), and a combination of PS and SBAS (Ferretti et al., 2011; Hooper, 2008). The first concentrates on the phase analysis of PS points using single master interferogram formation; in contrast, the second extracts information from distributed scatterer (DS) points with the aid of multi-master interferogram formation based on the small baseline constraint. The final is a hybrid methodology taking advantage of respective merits from PS and SBAS.

Past investigations have demonstrated that, in the permafrost environment of TP, the DS points are prevalent except for artificial structures, e.g. the embankment of Qinghai–Tibet Railway (Chen et al., 2012b). Consequently, in order to extract as much information as possible, SBAS was used for the evolution analysis of the active layer and permafrost. In total, 19 L-band ALOS PALSAR SLC images (acquired from June 2007 to December 2010) were employed to cover the Beiluhe experimental site, Hoh Xil natural reserve in TP of China. This study is the in-depth phase of Chen et al. (2012b): firstly, instead of the improved IPTA, the SBAS is applied to guarantee a higher spatial density of target points, which is beneficial for error mitigation as well as information extraction; second, by an extended environmental site including the Qinghai–Tibet Railway (QTR), the relationships of permafrost, geomorphological processes and anthropogenic activities are further explored in this study.

2. Study area and datasets

For easy accessibility and available ground-based measurements, the Beiluhe, Hoh Xil natural reserve, TP of China is selected as the experimental site (see Fig. 1). It extends from 92°16′ to 93°2′E and from 34°25′ to 34°55′N. In Fig. 1(a) the SAR swath (highlighted by the red parallelogram) superimposed on the optical image from Google Earth is shown. The temporal averaged amplitude SAR image in Fig. 1(b) shows the study site covered with a spatial extent of approximately 63×45 km^2. The QTR can be easily identified due to its strong backscattering characteristic. The topography of this site is composed by upland in the middle section in a NW–SE direction represented by Fenghuo and Ri'achi Mountains; and mild terrain in the northeast and southwest is represented by Beiluhe and Erdaogou valleys. The arid continental climate is due to the high elevation (4500–5200 m). Compared with the scarce precipitation (approximately 300–400 mm yr^{-1}), evaporation is much higher, resulting in arid conditions characterized by a negative water budget. However, Warm and Ice-Rich Permafrost (WIRP) is well developed in several sub-regions, particularly surrounding the two valleys with mild terrain, high soil moisture and relatively warm ground temperature (−1.8 to −0.5 °C) (Lin, Niu, Ge, Wang, & Dong, 2010). In comparison with other mountainous regions, the sub-surface temperature and ice-content of the active layer and permafrost beneath are both higher in the valley terraces; thawing islands could even exist through WIRP regions, particularly where rivers and geothermal heat flow.

19 ALOS PALSAR images acquired with ascending orbit and 34.3-degree nominal radar look angle, from June 2007 to December 2010, were used in this study, including 9 scenes of Fine Beam Single polarization (FBS, 28 MHz) and 10 scenes of Fine Beam Dual polarization (FBD, 14 MHz). Interested readers can refer to Chen et al. (2012b) for more details. The ALOS PALSAR data were obtained from the Japan Aerospace Exploration Agency (JAXA). In general, ALOS PALSAR has two advantages for the TP region monitoring: 1) PALSAR works with a longer wavelength (L-band, 23.6 cm), and hence penetrates vegetation better, resulting in high quality interferograms; and 2) the ground resolution of PALSAR (8 m of FBS and 16 m of FBD) is higher than other median resolution data (e.g. 25–30 m of ERS-1/2 and Envisat ASAR), and thus provided more detailed information. For the topographical data, 3-arcsecond Shuttle Radar Topography Mission (SRTM) DEM data from the United States Geological Survey (USGS) were used firstly for the topographic phase removal in DInSAR procedures, and then for InSAR products geocoding.

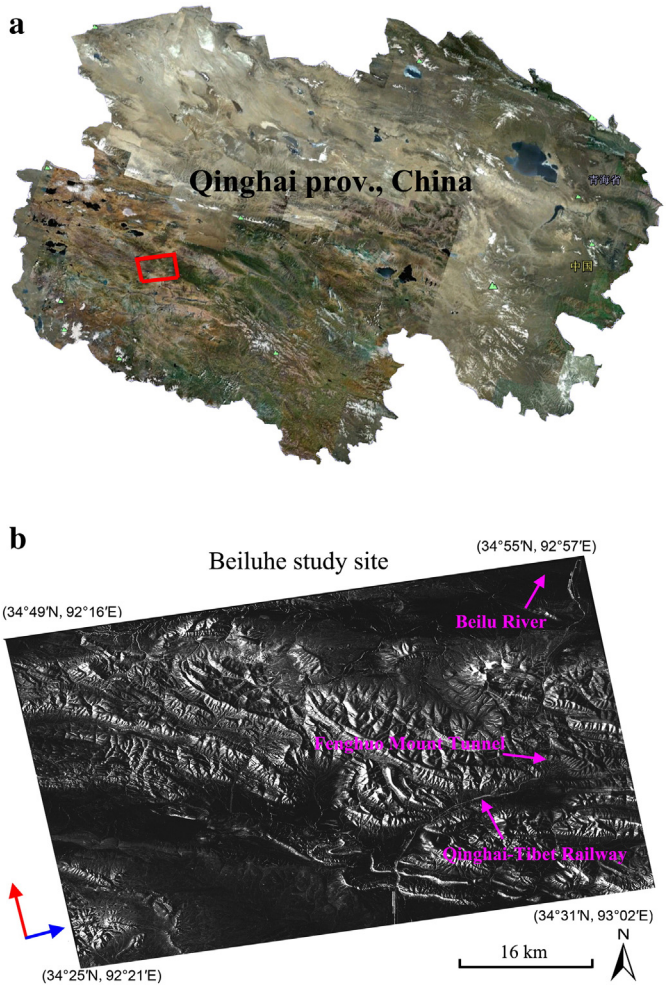

Fig. 1. (a) SAR swath (highlighted by the red parallelogram) superimposed on the optical image from Google Earth (GE). (b) Location of Beiluhe, Hoh Xil natural reserve in TP of China; the Qinghai–Tibet Railway is shown as strong backscatters; ALOS PALSAR flight paths and viewing directions are indicated by the red and blue arrows, respectively. (For interpretation of the references to color in this figure legend, the reader is referred to the web version of this article.)

3. SBAS procedures

Inspired by previous investigations (Rykhus & Lu, 2008; Short et al., 2011), InSAR measurements were introduced for surface deformation monitoring over permafrost environment in Beiluhe section, Hoh Xil natural reserve of TP. We found that seasonal effects and non-linear surface motions in this arid region were evident (Chen et al., 2012b). Except for geomorphological processes in slopes, we hypothesized that the surface deformation of TP was analogous to Alaska, USA as described by Liu, Zhang, and Wahr (2010), Liu, Schaefer, Zhang, and Wahr (2012); i.e. the surface movements were caused by two primary components: seasonal displacement by thaw settlement or frost heave of the active layer, and the secular subsidence due to the thawing of ice-rich permafrost near the permafrost table. Our past field investigations

indicated that apart from artificial structures, e.g. QTR (generally indicated as PS points), DS features were dominant over Hoh Xil natural reserve in TP. Consequently, in order to extract information on surface displacements (geomorphological processes, the combination dynamics of permafrost and the overlaid active layer), the SBAS method (Berardino et al., 2002) was used in order to take advantage of its capability for dense DS extraction and for identification of regions with significant movements.

In the SBAS approach, interferogram formation is controlled by the thresholds of spatial–temporal baselines as well as the Doppler centroid difference. In this study, considering that the Doppler centroid differences were negligible, only the spatial–temporal baselines were applied (smaller than 3800 m and 368 days to generate a connected graph). The common HH polarization data from two fine modes were used for interferometric processing after the FBS data were doubly downsampled in range direction. The multi-looking with 1 by 5 in range and azimuth direction (after doubly down-sampling of FBS data) were used to derive InSAR products with approximately 16 m ground resolution. 67 differential interferograms were generated after the removal of the topographic and flat earth phase components. The Minimum Cost Flow (MCF) method (Costantini, 1998) was used for phase unwrapping. After careful manual inspection, another 7 low-quality interferograms (including phase unwrapping and imprecise orbit errors) were discarded resulting in 60 final interferograms for further motion estimation and time series analysis (Fig. 2). The discarding procedure was conducted based on the two following hypotheses: 1) motion signatures on interferograms are primarily in the range of $[-\pi,+\pi]$ and are correlated spatially, particularly for neighborhood points; and 2) falsely phase unwrapping tends to occur in regions with low-coherence. Therefore, phase unwrapping errors are detected by discontinuous phase jumps particularly on those interferograms with low coherence, as well as the orbit errors are represented by the occurrence of regular fringes, primarily in range direction. It is clear that the PALSAR perpendicular baseline is correlated with the time of acquisition (Samsonov, 2010), implying the suitability of SBAS method for the TP investigation in the case of isolated interferogram subsets in time. In addition, taking advantage of SBAS, the small baseline formation further mitigates topographic errors before the estimation of parameters (e.g. residual height, displacements and atmospheric disturbance); in this study, majority of entire interferograms (more than 75%) have a perpendicular baseline less than 1500 m.

The implementation of SBAS can be realized by two main steps. 1) We estimated a temporal Low-Pass (LP) component of the motion signal and topographic artifacts via the least squares solution to separate the topographic and motion components using a preferred cubic displacement model. The Coherent Point (CP) candidates were characterized by a high average spatial coherence. And the reference point (showing a high coherence value of 0.92) was located on a stable subregion (flat and dominant with permanent permafrost and marked by the star in Fig. 3(a)). Following this operation, the estimated LP phase patterns and topographic artifacts were subtracted from wrapped differential interferograms, and then a new unwrapping step (Costantini, 1998) was implemented to the residual-wrapped phase patterns, resulting in improved results due to the reduced fringe rate. By adding back the subtracted LP phase component, we achieved a refined unwrapped differential phase pattern. 2) We estimated motion components using the Singular Value Decomposition (SVD) method by analyzing the refined unwrapped differential phase pattern (derived in step 1). Similar to other MT-InSAR approaches, we estimated atmospheric artifacts using the residual phase component (the motion component subtracts the LP phase pattern), which takes advantage of the characteristics of atmosphere in spatial–temporal domain; i.e. a high

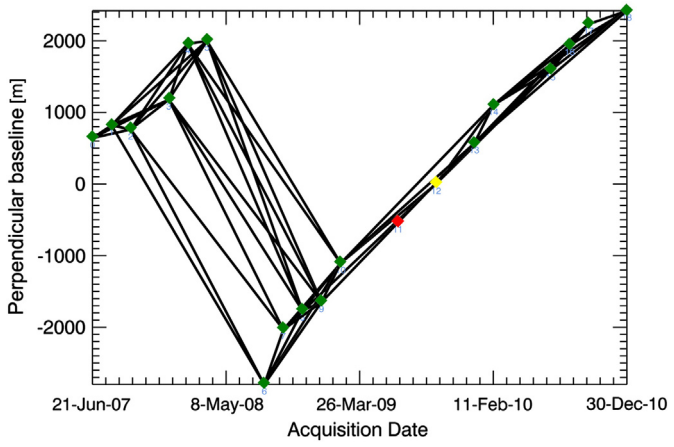

Fig. 2. Spatial–temporal distribution of interferogram formation based on the small baseline constraint. It is clear that the perpendicular baselines are correlated with the acquisition time. The number 12 image marked in yellow is the reference image acquired on 26 September 2009 for the dataset co-registration. The image marked in red is discarded because of its evident atmospheric or orbit error. (For interpretation of the references to color in this figure legend, the reader is referred to the web version of this article.)

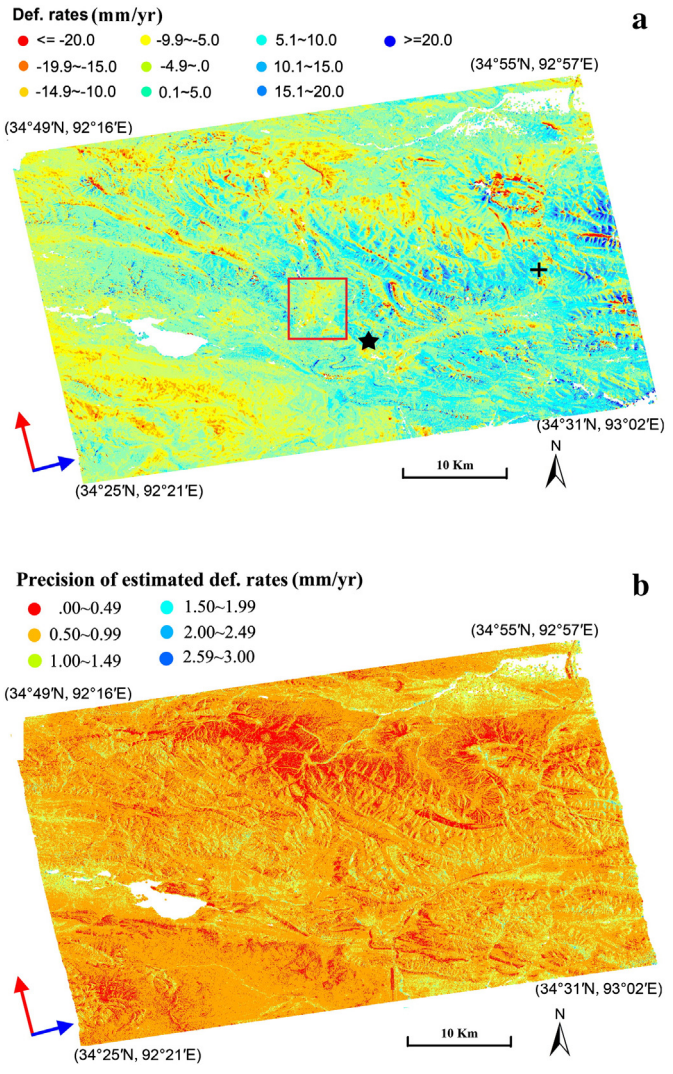

Fig. 3. (a) SBAS-derived surface displacement linear rates over Beiluhe, Hoh Xil natural reserve of TP in LOS direction based on the reference point (marked by the star). The red rectangle represents a slope in Fenghuo Mount; and the cross marks the location of leveling data (nearby the Fenghuo Mount Tunnel frontier) for SBAS results validation. (b) The precision of estimated displacement rates. The satellite was traveling in the direction of the red arrow and looking in the direction of the blue arrow. (For interpretation of the references to color in this figure legend, the reader is referred to the web version of this article.)

spatial correlation but a significant temporal decorrelation. We eventually achieved the motion phase after subtracting the atmospheric phase component. The final CPs were further identified by the temporal coherence defined by Eq. (16) of Pepe and Lanari (2006).

4. Results, validation and monitoring interpretation

Using the two thresholds (0.4 average spatial coherence and 0.7 temporal coherence), the SBAS derived surface displacement rates in line-of-sight (LOS) over Beiluhe section, Hoh Xil natural reserve of TP are illustrated in Fig. 3(a). The negative motion rates' sign is indicative of an increasing distance with time away from the satellite (subsidence); and positive sign represents an uplift motion. The result indicates that the surface motion in permafrost environment is evident, primarily in the range of -20 mm yr^{-1} to 20 mm yr^{-1} in the 3.5-yr observation period (from June, 2007 to December, 2010). Fig. 3(b) shows the precision of the estimated displacement rates. Those small values, in the range of 0 to 3 mm yr^{-1}, imply the reliability of estimated parameters. The InSAR-derived results have been validated by leveling data (from October, 2005 to December, 2009 with one month interval) located nearby the Fenghuo Mount Tunnel frontier (marked by the cross in Fig. 3(a) and plotted in Fig. 4). In order to minimize the location difference referring to the leveling benchmark, nearest neighbor comparison was employed. Then, the SBAS-derived deformation rate and time series were transformed from LOS into a vertical direction. The two different types of data demonstrate consistent motion trends with absolute discrepancies varying from 0.3 to 4.5 mm in the period from 21 June, 2007 to 19 December, 2009 (the overlap observations of two source data). The observed discrepancies are probably caused by: 1) the spatial–temporal difference of the two different types of data; and 2) the leveling observation error together with the SBAS data precision. Furthermore, seasonal non-linear motion trends are evident due to the frost heave and thawing settlement of the active layer, as illustrated in Fig. 4. There are totally 7,688,724 CPs over the study site with approximately 63 × 45 km^2, that is, 2712 CPs km^{-2}. The high spatial density of CPs is determined by the following two aspects. 1) PALSAR has a long wavelength, resulting in high penetration and coherence preservation, particularly in non-urban areas, for example in TP. 2) The small baseline strategy was introduced in interferometric formation, and thus high-quality interferograms were guaranteed, resulting in high spatial density of CP candidates and the final CPs.

In order to interpret the motion trends (magnitude and direction), particularly for slopes, the relationship between SAR imaging geometry (ascending with 34.3° viewing angle in this case) and the surface displacement was analyzed (see Fig. 5). With a few exceptions, the direction of surface movements fits expectations: the parallel movement, caused by widespread slope processes (e.g. general creep), was dominant in

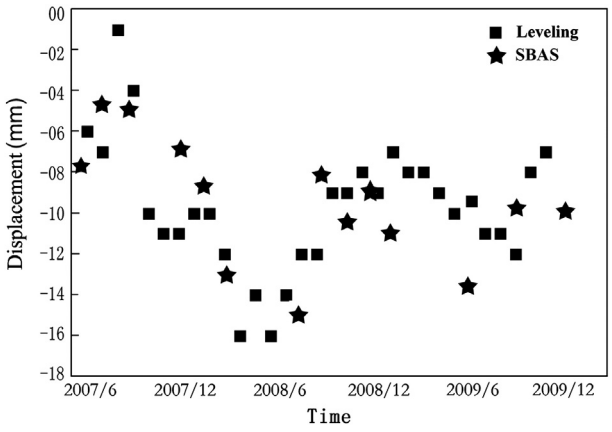

Fig. 4. Time series comparison between InSAR-derived measurements and leveling data, indicating consistent motion trends in the overlap observation period.

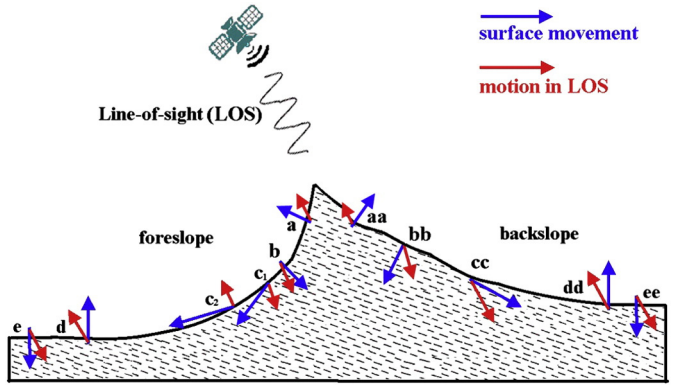

Fig. 5. The relationship between surface movements and InSAR detected displacements in LOS direction, particularly for mountainous regions.

the middle section of slopes; for other portions, the rotational motion was prevalently caused by the alluvial accumulation or the combination dynamics of permafrost and the overlaid active layer, such as the secular subsidence due to ice-rich permafrost thawing near the permafrost table. In the upper section of slopes, the rotational motions from both sides demonstrated consistent movements: frost heave as uplifts in LOS and thaw settlement as subsidence in LOS, shown as 'a', 'aa' and 'b', 'bb' in Fig. 5. For the slope facing the satellite, the downslope movement of material on the steep section (angle of gradient > 34.3°) indicated mild subsidence (marked by 'c_1') and on the moderate section (angle of gradient < 34.3°) showed mild uplift (marked by 'c_2'). In the backslopes, those two motion components were illustrative of obvious subsidence (see 'cc'). In valley regions with flat terrain (the foot of slopes), the actual motion trend from both sides could be seen as uplift (marked by 'd' and 'dd', respectively) when the deposition or heave was dominant, and as subsidence (marked by 'e' and 'ee', respectively) when the thaw settlement was prevalent.

From Fig. 3(a), it is clear that the majority of active layers (60% to 65%) were relatively stable during the 3.5-yr observation period, with displacements in the range of -5 mm yr^{-1} to 5 mm yr^{-1} (i.e. approximately twice the maximum precision value of estimated displacements). Significant movements occur in two cases, including in mountainous slopes and flat WIRP areas, and as evident from the visual interpretation of Figs. 1 and 3. In general, the residual topographic signal would be significant on differential interferograms in the case of large perpendicular baselines. However, this phenomenon only occurs on a small portion of the entire set of interferograms, namely 25% (15 in 60) used in this study. Moreover, the topographic phase component together with atmospheric disturbance have been estimated and canceled out using the SBAS algorithm of Berardino et al. (2002). The irrelevance of estimated motion rates and residual heights further implied the correctness of parameter estimation, based on which the mitigation of the topographic phase component could be implemented. With regard to the tropospheric stratification delay, firstly, the air in Tibet Plateau was thin (average height is more than 4500); secondly, the differential height in mountain areas was less than 500 m, resulting in errors quite consistent with the precision of motion signals. Thus the tropospheric stratification of atmospheric component can be neglected in this case. In summary, we interpreted that the correlation between InSAR results with topography is a convincing indicator for the geomorphological processes in play. In order to provide additional evidence, two representative high-resolution optical images from Google Earth were used to show the slope instability or physical slope processes (highly weathered and eroded; see Fig. 6). Note that due to the scattering mechanism, CPs cannot exist in radar shadow (no signature) or serious layover areas (mixed signatures from multi-features) and in accordance with the extraction rule for target points with high spatial–temporal coherence. The detected distinct uplifts (Fig. 3(a)) were highly related to geomorphological processes characteristic of slopes (see downward

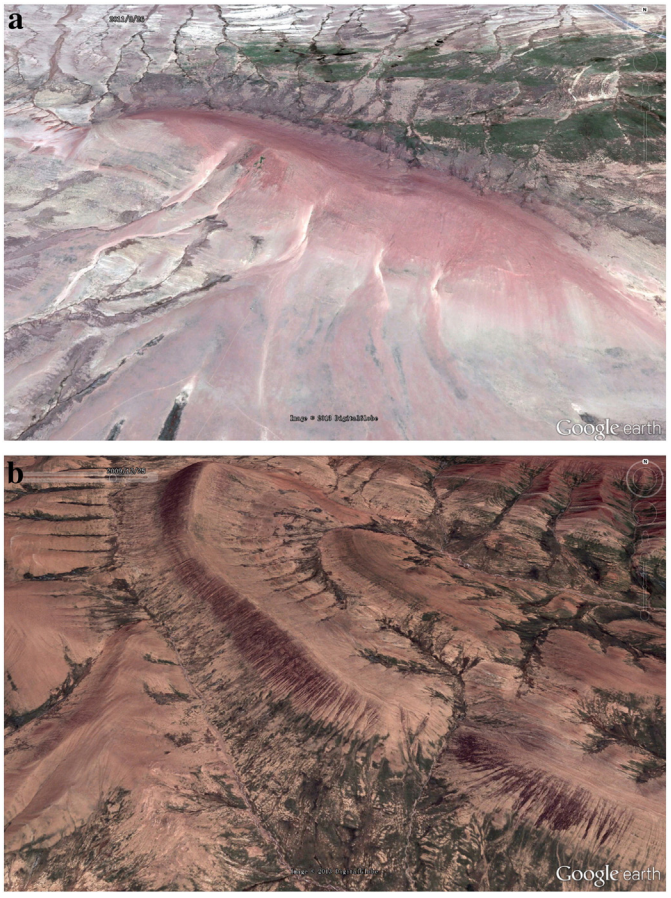

Fig. 6. Representative high-resolution optical images from Google Earth show the evident slope instability or physical slope processes (highly weathered and eroded).

movements of 'c_2' in Fig. 5) rather than due to permafrost or the active layer growth under climate warming trends. Furthermore, a few isolated uplifts (with values larger than 20 mm yr^{-1}) were located in high altitudinal mountains ('a' and 'aa' in Fig. 5). The remaining moderate-to-severe subsidence surface, with values in the range of −20 mm yr^{-1} to −5 mm yr^{-1}, corresponded to mountainous slopes or mild-terrain WRIP regions. The subsidence on backslopes was caused by the transitional movement of unconsolidated material linked to geomorphological processes ('cc' in Fig. 5). The distinct settlement on WRIP areas has been due to the combination of thaw settlement of the active layer as well as permafrost thawing near the permafrost table ('e' and 'ee' in Fig. 5).

Note that the tectonic motion in TP was not negligible as previously shown by Cavalie et al. (2008) and Loveless and Meade (2011). The nominally interseismic GPS velocities (relative to the stable Eurasia reference frame) in recent years demonstrated that the tectonic movement over Beiluhe section, Hoh Xil natural reserve of TP was around 15 mm yr^{-1} in a SW–NE direction (approximately perpendicular to the fight path of ALOS PALSAR). This introduced a systematic subsidence contribution in LOS direction with values in the range of −7 mm yr^{-1} to −8 mm yr^{-1} in the Beiluhe site. However, as we know, the SBAS results only measured the relative displacements compared with a local reference point, and thus this homogeneous bias was not taken into consideration when the study site coverage was smaller than 500 × 500 km^2.

5. Discussions

Liu et al. (2010) found that the causes of surface deformation over permafrost regions were complicated. At local scale, the deformation could be controlled by local surface vegetation, soil deposits, water/ice content, active layer thickness, hydrological settings etc. Secular surface subsidence could be another driving-force due to the thawing of ice-rich permafrost beneath the active layer due to global warming. Quantitative deformation discrimination of permafrost and overlaid active layer was beyond the scope of this paper. Interested readers may refer to Liu et al. (2010, 2012). However, the contributions to InSAR signals from geomorphological process and anthropogenic have been illustrated in this study and were further discussed.

5.1. Mountainous slopes

Past field investigations indicated that the vegetative cover in the Beiluhe site was relatively sparse; scattered alpine meadows occurred in flat valleys due to the relatively higher soil moisture. In the TP arid and cold environment, the mountains were covered by exposed rocks or weathered deposits. They were unconsolidated because of heavily decomposed rocks as well as sparse vegetation. Consequently, when

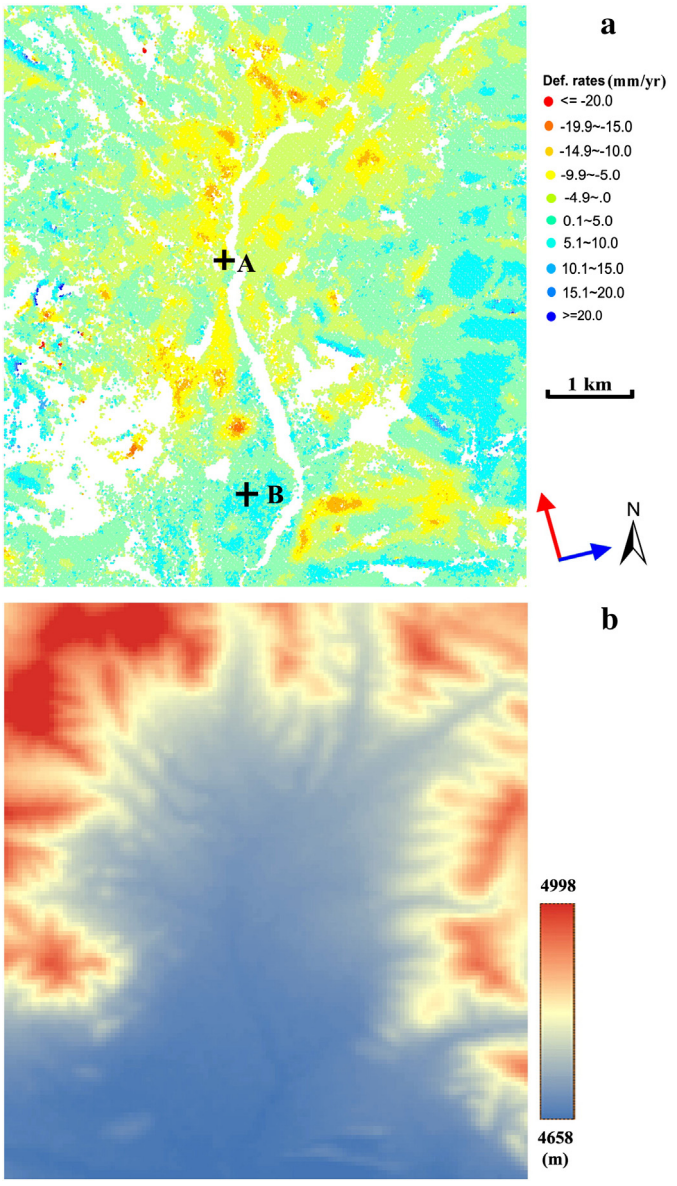

Fig. 7. Different motion mechanisms can be discriminated by InSAR measurements along a mountainous area with slopes. (a) Surface deformation linear rates overlapped on the optical image from Google Earth (GE); crosses 'A' and 'B' indicate two CP targets for the time series analysis, the red and blue arrows mark the satellite traveling and looking directions. (b) Relief shaded DEM. (For interpretation of the references to color in this figure legend, the reader is referred to the web version of this article.)

the shearing force (triggered by the surface overflow and shallow groundwater flow) exceeds a threshold, a shallow-seated landslide occurs. Fig. 7(a) showed the surface deformation field over a mountain region nearby Fenghuo Mountain. Referring to relief-shaded DEM in Fig. 7(b), it is clear that mild uplifts in LOS direction were dominated in the upper section of slopes primarily owing to frost heave ('a'–'aa' in Fig. 5). In the middle section of the fore-slope (slope gradient > 34.3°) and the middle-lower section of the backslope, the downward transitional movement, parallel to the bedrock beneath was evident, indicating moderate-to-high subsidence ('c_1'–'cc' in Fig. 5). The occurrence of the transitional movement in the lower section of the fore-slope and the deposit accumulation at the foot of both slopes jointly resulted in mild uplifts of InSAR measurements ('c_2' and 'd'–'dd' respectively in Fig. 5). In addition, the time series of two typical CPs ('A' and 'B' in Fig. 7) was further analyzed and the results were illustrated in Fig. 8. The seasonal variation was remarkable, revealing the influence of southeastern Asian monsoons (including summer and winter monsoons) as well as the seasonal displacement of the active layer due to frost heave and thaw settlement. The surface displacement over permafrost was complex and may not completely represent the evolution of permafrost; because other impacts, e.g. soil water phase change within the active layer, surface erosion as well as the tectonic movement, can all contribute to the surface displacement. However, in this case, the impacts from the tectonics and the permafrost evolution can be negligible: 1) the tectonic movement was uniform for a slope region, and thus this homogeneous bias can be canceled out considering the characteristic of SBAS data (relative measurement based on a local reference point); and 2) permafrost evolution was insensitive in a 3.5-yr observation span due to its long-term response (approximately 10 years or even longer). Therefore, apart from the seasonal displacement of the active layer induced by the frost heave and thaw settlement, the geomorphological processes in mountainous areas were dominant over other influences in the short 3.5-yr observation span. In summary, due to the sophisticated physical movements along slopes in Hoh Xil natural reserve of TP, more information with respect to topography (slope gradients and facing direction), geology (mantle composition and surface cover), hydrology (surface–subsurface runoff and permafrost ice-content melting) would be needed for the monitoring of active layer evolution (e.g. motion rates, directions and trends) as well as for interpretation of causal factors (rainfall, the active layer and permafrost dynamics).

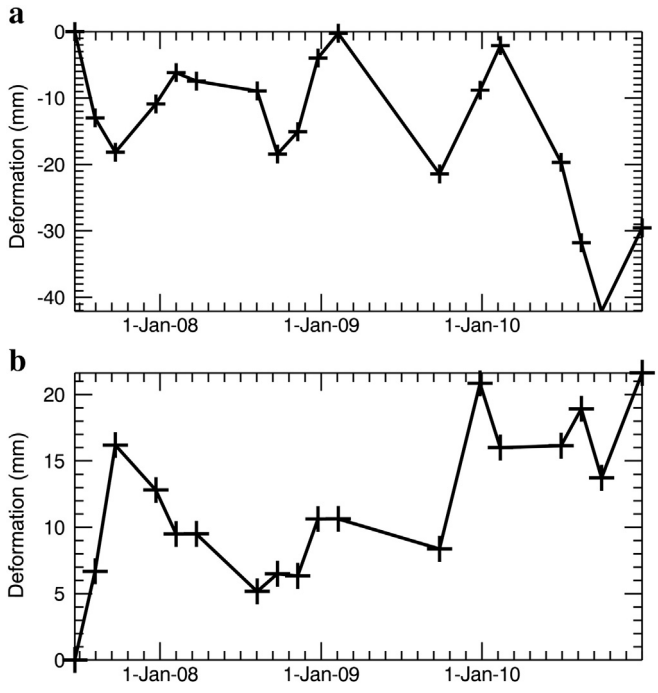

Fig. 8. Displacement time series of two typical CP targets (marked by crosses in Fig. 7); (a) the subsidence, and (b) the uplift. The seasonal variation is obvious.

5.2. Qinghai–Tibet Railway (QTR)

The QTR project is a 100-yr grand plan; therefore its embankment instability needs to be well monitored to avoid potential geo-hazards. The embankment deformation surveillance has been covered by recent studies (Li, Lai, Zhang, & Dong, 2009; Zhang, Zhang, & Qin, 2010). The SBAS-derived surface deformations along the embankment of QTR in Beiluhe section, Hoh Xil natural reserve of TP, China were illustrated in Fig. 9(a). Except for few uplifts due to proactive "cooling down" measures (Yu, Niu, Pan, Bai, & Zhang, 2008; Fig. 9(b)), the surface subsidence along the embankment of QTR was primarily in the range of -25 mm yr^{-1} to -10 mm yr^{-1}. This was probably caused by the combination of the increased compression settlement, destroyed active layer as well as depressed soil heat release. In general, the QTR runs through mild-terrain valleys to enhance the construction feasibility of the embankment, bringing in the challenges of surface vulnerability caused by the co-occurrence of WIRP regions. Human activities, e.g. the embankment construction, easily break the original balance of the active layer, resulting in remarkable settlements due to the following aspects: 1) the train-induced compression and the temperature increment of sub-surface jointly speed up the thawing settlement of the active layer in a short period (approximately 5–10 years); and 2) over the long-term, the secular subsidence due to thawing of ice-rich permafrost triggered by anthropogenic activities could be another factor, particularly under global warming. The motion trend of the embankment along the QTR has been explored by the improved Interferometric Point Target Analysis (IPTA) approach in our previous study (Chen et al., 2012b). The comparison between SBAS and improved IPTA-derived results along the Beiluhe Bridge section was shown in Fig. 10. It is obvious that fake target points in deformation rate fields due to error phase unwrapping have been mitigated owing to the merit of SBAS, resulting in easy identification of potentially risky sections (represented by serious surface settlement with orange-red colors) as well as the effect of cooling-down measures (represented by stable or mild uplift, and also marked by the black arrow in Fig. 10); all of the information were indeed valuable for the management of the QTR embankment. Furthermore, compared with the improved IPTA in Fig. 10(b), the spatial density of CP points has been significantly enhanced in this study, nearly one order magnitude better than the previous one; that is, approximately 2200 CPs km^{-2} vs. 280 PSs km^{-2}. This improvement not only physically avoids phase unwrapping errors, but also is beneficial for the displacement analysis in detail. The QTR section with cooling-down ventiducts was clearly distinguishable, as marked by black arrows in Fig. 9(a) and Fig. 10(a); however, not discriminating for the improved IPTA in Fig. 10(b). Generally, an inconsistent spatial motion is more risky than a uniform trend, because it brings in ruptures, distortions or other defected deformations. Consequently, the information related to transition boundaries of inverse motion trends were imperative for policymakers. Thanks to the enhanced density of CP targets of SBAS, the spatial distribution of displacements (settlement or uplift) along the QTR was apparent, as illustrated in Fig. 10(a), providing potential hot-spots which require further examination as a priority.

6. Conclusions

In this study, taking the Beiluhe section, Hoh Xil natural reserve of TP, China as the experimental site, we examined the relationship of the active layer evolution, geomorphological processes and anthropogenic activities through InSAR approaches. Apart from the probable tectonic activity, SBAS derived results indicated that the movement of most active layers overlaid on the permafrost was relatively stable during the 3.5-yr short observation period, ranging from -5 mm yr^{-1} to 5 mm yr^{-1} in LOS direction. In contrast, significant displacements

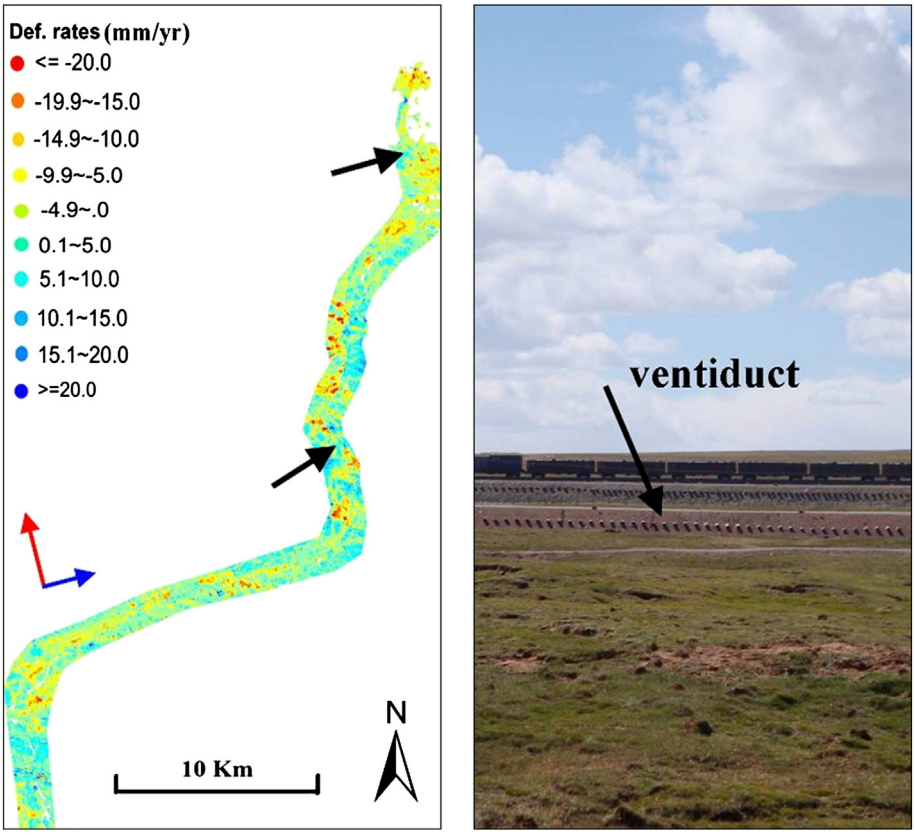

Fig. 9. (a) Surface deformations along the embankment of QTR in Beiluhe section, Hoh Xil natural reserve of TP, China. The red and blue arrows mark the satellite traveling and looking directions. The mild uplift patches due to cooling measures are marked by black arrows. (b) Cooling-down measure of ventiducts along the embankment of QTR.

occurred in mountainous and WRIP regions. Displacements in mountainous areas were highly related to the geomorphological processes on those unconsolidated, weathered slope mantles triggered by seasonally heavy monsoonal rains. For WRIP regions, displacements were caused by the dynamics of the active layer and the permafrost beneath; under global warming, the surface over WIRP regions would be unstable due to the

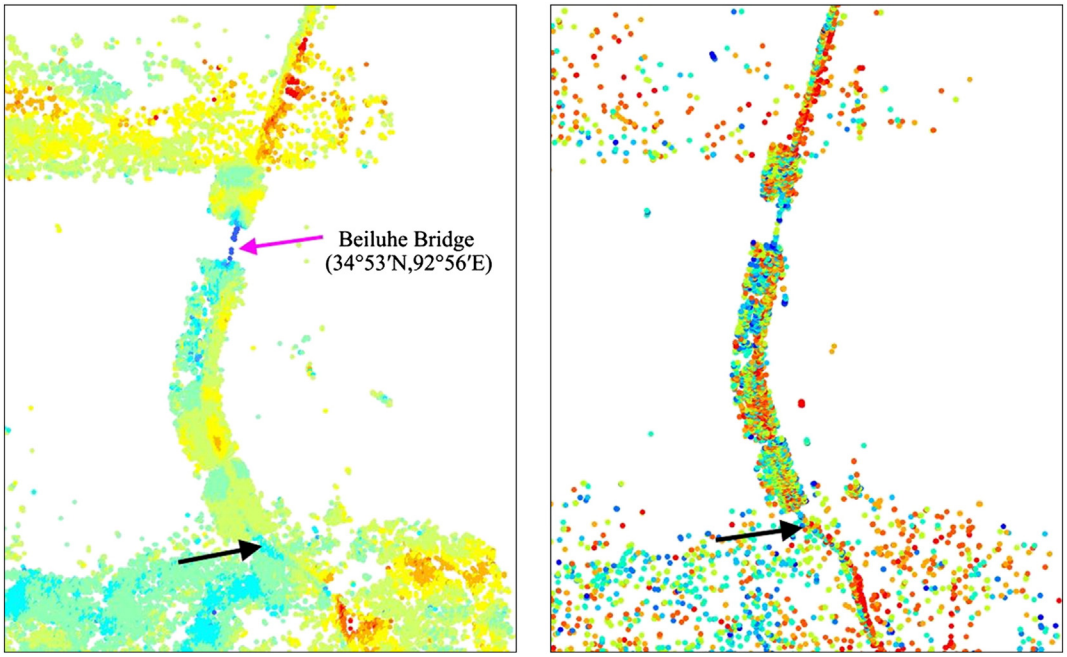

Fig. 10. Comparison of displacement annual rates between the improved IPTA (Chen et al., 2012b) and the SBAS in this study. (a) SBAS, and (b) improved IPTA. The black and pink arrows indicate the locations of the cooling-down ventiduct and Beiluhe Bridge, respectively. (For interpretation of the references to color in this figure legend, the reader is referred to the web version of this article.)

thawing settlement of the active layer as well as the ice-rich permafrost beneath. The main conclusions of this work can be summarized as follows:

1) Instead of persistent scatterer points, the CP targets in the permafrost environment are evident; this phenomenon determines the feasibility of SBAS. Totally 7,688,724 CPs over the study site (63×45 km^2) were extracted with the temporal coherence threshold of 0.7, that is, 2712 CPs km^{-2}. The majority of land covers were identified as DS targets (see Figs. 1 and 3), except for the water body (e.g. Beilu River) and sandy-bare ground around the Beiluhe valley because of mirror scattering. The high density of DSs was jointly determined by the small baseline interferometric formation and L-band long wavelength of ALOS PALSAR data. In addition, the isolated interferogram clusters in the time domain (due to the corrective satellite orbit maneuver of PALSAR) further supports the suitability of SBAS for this study.
2) The movement of the overlaying active layer in slopes was more remarkable compared with other natural scenarios. This phenomenon was primarily due to the erosion on unconsolidated surface triggered by heavy rainfalls in summer due to the southeastern Asian monsoons. Furthermore, the motion trend indicated a notable seasonal variation, implying seasonal thaw settlements and frost heave of the active layer. The slopes in this arid and cold region were covered by heavily weathered mantles with bare or sparse vegetation. The stability was vulnerable under the external driving-force from intense rainfalls, resulting in landslides. The hypothesis model of surface movements in slopes has been interpreted (Figs. 5 and 7); that is, the transitional motion was dominant in the middle section, and then gradually transformed into rotational displacement due to deposit accumulation at the foot of slopes.
3) The QTR and its neighborhood were suffering from more obvious surface subsidence than surrounding features (in the range of -25 mm yr^{-1} to -10 mm yr^{-1}). This phenomenon revealed the human activity impact on the evolution of the active layer as well as the permafrost, particularly in WIRP regions: Firstly, geological conditions as well as the land cover along the embankment have been changed during the construction, resulting in aggravated active layer erosion and remarkable surface settlements due to the thawing impact from the active layer and permafrost. Secondly, the compression of the underlying permafrost soil has been accelerated from the downward pressure induced by the rocky foundation as well as running trains, particularly in a short-term (within 5 years) after the QTR's operation. Last but not the least, the moisture–heat balance between the active layer and air has been destroyed; resulting in thaw subsidence due to the raised sub-surface temperature, particularly under global warming.

In order to derive interferograms with high quality, multi-looking was applied at the cost of some loss of spatial resolution. More recently, several innovative methods (Ferretti et al., 2011; Hooper, 2008) have been proposed by synergistically using persistent scatterer and DS to increase the spatial density of detected targets in natural areas and simultaneously preserving the original spatial resolution. We intend to investigate the use of those new methods in the Hoh Xil natural reserve of TP in the future; using high-resolution, newly-launched spaceborne SAR systems (e.g. TerraSAR-X, Cosmo-SkyMed and Radarsat-2) to extract more accurate seasonal motions and corresponding time series, taking advantage of shorter revisit cycles (Bovenga, Wasowski, Nitti, Nutricato, & Chiaradia, 2012), can also contribute to improving future studies.

Acknowledgment

This study has been supported by funding from the National Natural Science Foundation of China (41201455), the Research Grants Council of the HKSAR, China (450210), the Innovation and Technology Support Programme of HKSAR, China (ITS/152/11FP), and the Hundred Talents Program of the Institute of Remote Sensing and Digital Earth, Chinese Academy of Sciences (Y2ZZ27101B). We thank the Associate Editor and anonymous reviewers for their constructive and insightful comments. The digital elevation model of the investigated zone was acquired through the SRTM archive. The original ALOS PALSAR data were provided by the Japan Aerospace Exploration Agency (JAXA).

References

Berardino, P., Fornaro, G., Lanari, R., & Sansosti, E. (2002). A new algorithm for surface deformation monitoring based on small baseline differential SAR interferograms. *IEEE Transactions on Geoscience and Remote Sensing*, *40*(11), 2375–2383.

Bovenga, F., Wasowski, J., Nitti, D. O., Nutricato, R., & Chiaradia, M. T. (2012). Using COSMO/SkyMed X-band and ENVISAT C-band SAR interferometry for landslides analysis. *Remote Sensing of Environment*, *119*, 272–285.

Cavalie, O., Lasserre, C., Doin, M. -P., Peltzer, G., Sun, J., Xu, X., et al. (2008). Measurement of interseismic strain across the Haiyuan fault (Gansu, China), by InSAR. *Earth and Planetary Science Letters*, *275*, 246–257.

Chen, F., & Lin, H. (2011). Multi-baseline differential SAR interferometry analysis of Lantau Highway, Hong Kong, using Envisat ASAR data. *Remote Sensing Letters*, *2*(2), 167–173.

Chen, F., Lin, H., Li, Z., Chen, Q., & Zhou, J. (2012a). Interaction between permafrost and infrastructure along the Qinghai–Tibet Railway detected via jointly analysis of C- and L-band small baseline SAR interferometry. *Remote Sensing of Environment*, *123*, 532–540.

Chen, F., Lin, H., Yeung, K., & Cheng, S. (2010). Detection of slope instability in Hong Kong based on multi-baseline differential SAR interferometry using ALOS PALSAR data. *GIScience and Remote Sensing*, *47*, 208–220.

Chen, F., Lin, H., Zhang, Y., & Lu, Z. (2012b). Ground subsidence geo-hazards induced by rapid urbanization: Implications from InSAR observation and geological analysis. *Natural Hazards Earth System Science*, *12*, 935–942.

Costantini, M. (1998). A novel phase unwrapping method based on network programming. *IEEE Transactions on Geoscience and Remote Sensing*, *36*, 813–821.

Ferretti, A., Fumagalli, A., Novali, F., Prati, C., Rocca, F., & Rucci, A. (2011). A new algorithm for processing interferometric data-stacks: SqueeSAR. *IEEE Transactions on Geoscience and Remote Sensing*, *49*, 3460–3470.

Ferretti, A., Prati, C., & Rocca, F. (2000). Nonlinear subsidence rate estimation using persistent scatterers in differential SAR interferometry. *IEEE Transactions on Geoscience and Remote Sensing*, *38*, 2202–2212.

Guo, L. D., & Macdonald, R. W. (2006). Source and transport of terrigenous organic matter in the upper Yukon River: Evidence from isotope (delta C-13, Delta C-14, and delta N-15) composition of dissolved, colloidal, and particulate phases. *Global Biogeochemical Cycles*, *20*(GB2011), 12.

Hooper, A. (2008). A multi-temporal InSAR method incorporating both persistent scatterer and small baseline approaches. *Geophysical Research Letters*, *35*, 1–5.

Hooper, A., Bekaert, D., Spaans, K., & Arkan, M. (2012). Recent advances in SAR interferometry time series analysis for measuring crustal deformation. *Tectonophysics*, *514–517*, 1–13.

Hooper, A., Zebker, H., Segall, P., & Kampes, B. (2004). A new method for measuring deformation on volcanoes and other natural terrains using InSAR persistent scatterers. *Geophysical Research Letters*, *31*, L23611, http://dx.doi.org/10.1029/2004GL021737.

Immerzeel, W., Stoorvogel, J., & Antle, J. (2008). Can payments for ecosystem services secure the water tower of Tibet? *Agricultural Systems*, *96*, 52–63.

Ismail-Zadeh, A., Mouel, J. L. L., Soloviev, A., Tapponnier, P., & Vorovieva, I. (2007). Numerical modeling of crustal block-and-fault dynamics, earthquakes and slip rates in the Tibet–Himalayan region. *Earth and Planetary Science Letters*, *258*, 465–485.

Jiang, L., Lin, H., Ma, J., Kong, B., & Wang, Y. (2011). Potential of small-base SAR interferometry for monitoring land subsidence related to underground coal fires: Wuda (Northern China) case study. *Remote Sensing of Environment*, *115*, 257–268.

Jin, H., Yu, Q., Wang, S., & Lu, L. (2008). Changes in permafrost environments along the Qinghai–Tibet engineering corridor induced by anthropogenic activities and climate warming. *Cold Regions Science and Technology*, *53*, 317–333.

Kang, S., Xu, Y., You, Q., Flugel, W., Pepin, N., & Yao, T. (2010). Review of climate and cryospheric change in the Tibetan Plateau. *Environmental Research Letters*, *5*(015101), http://dx.doi.org/10.1088/1748-9326/5/1/015101 (8 pp.).

Lanari, R., Mora, O., & Manunta, M. (2004). A small-baseline approach for investigating deformations on full-resolution differential SAR interferograms. *IEEE Transactions on Geoscience and Remote Sensing*, *42*, 1377–1386.

Li, S., Lai, Y., Zhang, M., & Dong, Y. (2009). Study on long-term stability of Qinghai–Tibet Railway embankment. *Cold Regions Science and Technology*, *57*, 139–147.

Lin, H., Chen, F., & Zhao, Q. (2011). Land deformation monitoring using coherent target-neighborhood networking method combined with polarimetric information: A case study of Shanghai, China. *International Journal of Remote Sensing*, *32*, 2395–2407.

Lin, Z., Niu, F., Ge, J., Wang, P., & Dong, Y. (2010). Variation characteristics of the thawing lake in permafrost regions of the Tibetan Plateau and their influence on the thermal state of permafrost. *Journal of Glaciology and Geocryology*, *32*(2), 341–350.

Liu, L., Schaefer, K., Zhang, T., & Wahr, J. (2012). Estimating 1992–2000 average active layer thickness on the Alaskan North Slope from remotely sensed surface subsidence. *Journal of Geophysical Research - Earth Surface*, *117*, F01005, http://dx.doi.org/10.1029/2011JF002041.

Liu, J., Wang, S., Yu, S., Yang, D., & Zhang, L. (2009). Climate warming and growth of high-elevation inland lakes on the Tibetan Plateau. *Global and Planetary Change*, *67*, 209–217.

Liu, L., Zhang, T., & Wahr, J. (2010). InSAR measurements of surface deformation over permafrost on the North Slope of Alaska. *Journal of Geophysical Research - Earth Surface*, *115*, F03023, http://dx.doi.org/10.1029/2009JF001547.

Loveless, J. P., & Meade, B. J. (2011). Partitioning of localized and diffuse deformation in the Tibetan Plateau from joint inversions of geologic and geodetic observations. *Earth and Planetary Science Letters*, *303*, 11–24.

Massonnet, D., Rossi, M., Carmona, C., Adragna, F., Peltzer, G., Feigl, K., et al. (1993). The displacement field of the Landers earthquake mapped by radar interferometry. *Nature*, *364*, 138–142.

Monastersky, R. (2011). Permafrost science heats up in the United States. *Nature*, http://dx.doi.org/10.1038/nature.2011.9681.

Niu, F., Lin, Z., Liu, H., & Lu, J. (2011). Characteristics of thermokarst lakes and their influence on permafrost in Qinghai–Tibet Plateau. *Geomorphology*, *132*, 222–233.

Pepe, A., & Lanari, R. (2006). On the extension of the minimum cost flow algorithm for phase unwrapping of multitemporal differential SAR interferograms. *IEEE Transactions on Geoscience and Remote Sensing*, *44*, 2374–2383.

Qiao, X., Yang, S., Du, R., Ge, L., & Wang, Q. (2011). Coseismic slip from the 6 October 2008, Mw6.3 Damxung Earthquake, Tibetan Plateau, constrained by InSAR observations. *Pure and Applied Geophysics*, *168*, 1749–1758.

Rykhus, R. P., & Lu, Z. (2008). InSAR detects possible thaw settlement in the Alaskan Arctic Coastal Plain. *Canadian Journal of Remote Sensing*, *34*(2), 100–112.

Samsonov, S. (2010). Topographic correction for ALOS PALSAR interferometry. *IEEE Transactions on Geoscience and Remote Sensing*, *48*(7), 3020–3027.

Schuur, E. A. G., Bockheim, J., Canadell, J. G., Euskirchen, E., Field, C. B., Goryachkin, S. V., et al. (2008). Vulnerability of permafrost carbon to climate change: Implications for the global carbon cycle. *BioScience*, *58*, 701–714.

Short, N., Brisco, B., Couture, N., Pollard, W., Murnaghan, K., & Budkewitsch, P. (2011). A comparison of TerraSAR-X, RADARSAT-2 and ALOS-PALSAR interferometry for monitoring permafrost environments, case study from Herschel Island, Canada. *Remote Sensing of Environment*, *155*(12), 3491–3506.

Tarnocai, C., Canadell, J. G., Schuur, E. A. G., Kuhry, P., Mazhitova, G., & Zimov, S. (2009). Soil organic carbon pools in the northern circumpolar permafrost region. *Global Biogeochemical Cycles*, *23*, GB2023, http://dx.doi.org/10.1029/2008GB003327.

Usai, S., & Klees, R. (1999). SAR interferometry on a very long time scale: A study of the interferometric characteristics of man-made features. *IEEE Transactions on Geoscience and Remote Sensing*, *37*(4), 2118–2123.

Wang, G., Hu, H., & Li, T. (2009a). The influence of freeze–thaw cycles of active soil layer on surface runoff in a permafrost watershed. *Journal of Hydrology*, *375*, 438–449.

Wang, G., Li, S., Hu, H., & Li, Y. (2009b). Water regime shifts in the active soil layer of the Qinghai–Tibet Plateau permafrost region, under different levels of vegetation. *Geoderma*, *149*, 280–289.

Wu, Q., Jiang, G., & Zhang, P. (2010). Assessing the permafrost temperature and thickness conditions favorable for the occurrence of gas hydrate in the Qinghai–Tibet Plateau. *Energy Conversion and Management*, *51*, 783–787.

Wu, Q., & Zhang, T. (2008). Recent permafrost warming on the Qinghai–Tibetan Plateau. *Journal of Geophysical Research*, *11*, D13108, http://dx.doi.org/10.1029/2007JD009539.

Wu, Q., & Zhang, T. (2010). Changes in active layer thickness over the Qinghai–Tibetan Plateau from 1995–2007. *Journal of Geophysical Research*, *115*, D09107, http://dx.doi.org/10.1029/2009JD012974.

Yang, M., Wang, S., Yao, T., Gou, X., Lu, A., & Guo, X. (2004). Desertification and its relationship with permafrost degradation in Qinghai–Xizang (Tibet) plateau. *Cold Regions Science and Technology*, *39*, 47–53.

Yu, Q., Niu, F., Pan, X., Bai, Y., & Zhang, M. (2008). Investigation of embankment with temperature-controlled ventilation along the Qinghai–Tibet Railway. *Cold Regions Science and Technology*, *53*, 193–199.

Zhang, B., Zhang, J., & Qin, Y. (2010). Investigation for the deformation of embankment underlain by warm and ice-rich permafrost. *Cold Regions Science and Technology*, *60*, 161–168.